

# Molecular-level insights into CO<sub>2</sub> activation on Ni(111) from in situ infrared spectroscopy

B. Eren, A. Head

To be published in "Cell Reports Physical Science"

April 2024

Center for Functional Nanomaterials  
**Brookhaven National Laboratory**

**U.S. Department of Energy**

USDOE Office of Science (SC), Basic Energy Sciences (BES). Scientific User Facilities (SUF)

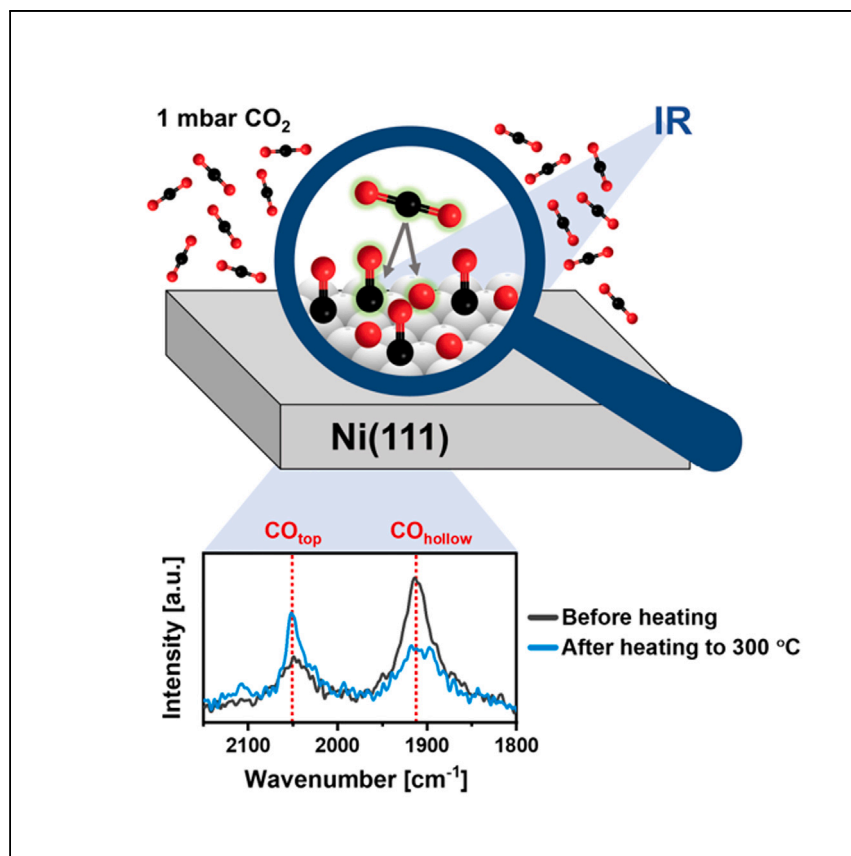
Notice: This manuscript has been authored by employees of Brookhaven Science Associates, LLC under Contract No. DE-SC0012704 with the U.S. Department of Energy. The publisher by accepting the manuscript for publication acknowledges that the United States Government retains a non-exclusive, paid-up, irrevocable, world-wide license to publish or reproduce the published form of this manuscript, or allow others to do so, for United States Government purposes.

## **DISCLAIMER**

This report was prepared as an account of work sponsored by an agency of the United States Government. Neither the United States Government nor any agency thereof, nor any of their employees, nor any of their contractors, subcontractors, or their employees, makes any warranty, express or implied, or assumes any legal liability or responsibility for the accuracy, completeness, or any third party's use or the results of such use of any information, apparatus, product, or process disclosed, or represents that its use would not infringe privately owned rights. Reference herein to any specific commercial product, process, or service by trade name, trademark, manufacturer, or otherwise, does not necessarily constitute or imply its endorsement, recommendation, or favoring by the United States Government or any agency thereof or its contractors or subcontractors. The views and opinions of authors expressed herein do not necessarily state or reflect those of the United States Government or any agency thereof.

Article

# Molecular-level insights into CO<sub>2</sub> activation on Ni(111) from *in situ* infrared spectroscopy



The adsorption and activation of carbon dioxide on nickel is a fundamental step in carbon dioxide conversion reactions. Here, Ben David et al. shed light on the dissociative adsorption of carbon dioxide on Ni(111) under ambient conditions and the atomistic mechanisms that affect the adsorption sites of CO intermediates.

Roey Ben David, Ashley R. Head, Senpeng Lin, Adva Ben Yaacov, Miguel A. Andres, Baran Eren

baran.eren@weizmann.ac.il

### Highlights

CO<sub>2</sub> undergoes direct dissociation on Ni(111), producing CO and atomic oxygen

A competitive adsorption mechanism dictates the site distribution of CO intermediates

The distribution of CO between top and hollow sites depends on sample temperature

Residual gases affect the oxidation state of Ni(111) at ambient CO<sub>2</sub> pressures

Ben David et al., Cell Reports Physical Science 5, 101890

April 17, 2024 © 2024 The Author(s).

<https://doi.org/10.1016/j.xcrp.2024.101890>



## Article

Molecular-level insights into CO<sub>2</sub> activation on Ni(111) from *in situ* infrared spectroscopyRoey Ben David,<sup>1</sup> Ashley R. Head,<sup>2</sup> Senpeng Lin,<sup>1,3</sup> Adva Ben Yaacov,<sup>1</sup> Miguel A. Andres,<sup>1</sup> and Baran Eren<sup>1,4,\*</sup>

## SUMMARY

The activation of CO<sub>2</sub> on nickel surfaces is the first step of various CO<sub>2</sub> conversion processes. Consequently, understanding the surface intermediates formed during this step and their adsorption sites is crucial for elucidating reaction mechanisms. In this study, we employ *in situ* infrared spectroscopy to investigate the interaction of 1 mbar CO<sub>2</sub> with a model Ni(111) catalyst between 25°C and 300°C. Under these conditions, CO<sub>2</sub> is activated via a direct dissociation into CO and atomic oxygen, while the oxidation state of the Ni(111) surface is primarily determined by residual H<sub>2</sub> and O<sub>2</sub>. The high surface coverage of CO and oxygen at ambient CO<sub>2</sub> pressure induces a competitive adsorption mechanism on the energetically favored hollow sites. This mechanism leads to a temperature-dependent distribution of CO between top and hollow sites, potentially explaining the effect of reaction conditions on the adsorption site of CO intermediates in CO<sub>2</sub> conversion reactions.

## INTRODUCTION

The adsorption and activation of CO<sub>2</sub> on metal surfaces are elementary steps to consider for the rational design of catalytic systems for CO<sub>2</sub> conversion and utilization via heterogeneous catalysis.<sup>1–3</sup> The most important CO<sub>2</sub> conversion reactions are CO<sub>2</sub> reduction to CO,<sup>4</sup> dry methane reforming (DMR),<sup>5–7</sup> and, perhaps most essentially, CO<sub>2</sub> hydrogenation.<sup>8–10</sup> CO<sub>2</sub> hydrogenation can proceed along three main pathways, classified by the resulting product: methanol, methane (the Sabatier reaction), and hydrocarbons (via Fischer-Tropsch synthesis and a CO intermediate). These reactions can occur by heterogeneous catalysis in the gas phase or liquid phase, sometimes assisted by photochemical and electrochemical processes. In the case of catalytic conversion of gas-phase CO<sub>2</sub>, the initial adsorption and interaction of CO<sub>2</sub> molecules with the catalyst surface are the pivotal steps that can affect subsequent reaction pathways and, thereby, the selectivity toward desired products.

Active metals commonly used for catalytic conversion of CO<sub>2</sub> include platinum-group metals (PGMs) such as Rh, Ru, Pt, Ir, and Pd as well as base metals like Ni, Co, and Cu. From an economic standpoint, base metals are preferable for large-scale industrial processes compared with PGMs. Ni-based catalysts are considered efficient materials for several CO<sub>2</sub> conversion reactions, such as DMR, CO<sub>2</sub> methanation, and CO<sub>2</sub> conversion to CO via the reverse water gas shift (RWGS) reaction.<sup>11–15</sup> The commonly accepted mechanisms of these reactions involve the molecular adsorption of CO<sub>2</sub> followed by charge transfer from the metal to form anionic bent CO<sub>2</sub><sup>δ−</sup>, which serves as a short-lived precursor state for direct dissociation into CO and atomic oxygen.<sup>16–19</sup> However, in the presence of hydrogen on the

<sup>1</sup>Department of Chemical and Biological Physics, Weizmann Institute of Science, 234 Herzl Street, Rehovot 76100, Israel

<sup>2</sup>Center for Functional Nanomaterials, Brookhaven National Laboratory, Upton, NY 11973, USA

<sup>3</sup>Department of Chemistry, Zhejiang University, Hangzhou 310058, China

<sup>4</sup>Lead contact

\*Correspondence: [baran.eren@weizmann.ac.il](mailto:baran.eren@weizmann.ac.il)  
<https://doi.org/10.1016/j.xcrp.2024.101890>



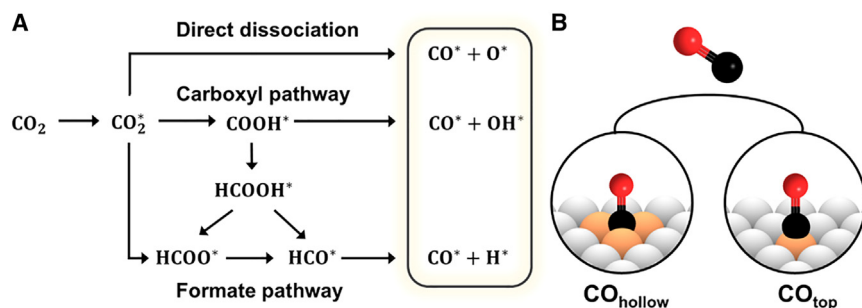


**Figure 1. CO<sub>2</sub> activation pathways on Ni**

(A) Schematic of CO<sub>2</sub> adsorption and dissociation on Ni via either direct dissociation or H-assisted dissociation through carboxyl (COOH\*) and/or formate (HCOO\*) intermediates.<sup>20</sup> (B) Schematic of the possible adsorption sites of CO on Ni(111).

surface, alternative H-assisted dissociation pathways through carboxyl (COOH\*) or formate (HCOO\*) intermediates are also possible.<sup>16,20–23</sup> These pathways, summarized in the theoretical work of Mohan et al.,<sup>20</sup> are presented in Figure 1A. The source of hydrogen atoms on the surface is the dissociative adsorption of H<sub>2</sub> gas for CO<sub>2</sub> methanation and RWGS reactions and CH<sub>4</sub> dehydrogenation for DMR. Both theoretical and experimental studies generally agree that the direct dissociation of CO<sub>2</sub> is energetically favored over the H-assisted routes, particularly on the (111) facets of Ni.<sup>20,23–25</sup> After the formation of CO intermediates, further decomposition can proceed via a direct dissociation to C\* and O\* or H-assisted dissociation via HCO\* or COH\* intermediates. For Ni(111), recent computational studies have shown that the direct dissociation of CO (i.e., without hydrogen) is not plausible due to a relatively high energy barrier (274–288 kJ/mol).<sup>20,23,25</sup> Therefore, it is more likely that CO would desorb from the surface rather than undergoing further dissociation.

The adsorption site of CO is one of the key parameters for reaction mechanisms involving the formation of CO intermediates. For example, on Ni(111), there are two potential adsorption sites: 3-fold hollow sites and top sites (Figure 1B). The 3-fold hollow sites can be further divided into face-centered cubic (fcc) and hexagonal close-packed (hcp) sites, but the difference in adsorption energy between them is estimated to be negligible (~3 kJ/mol).<sup>17,26</sup> On the other hand, the calculated adsorption energy of CO on hollow sites (–183 kJ/mol) is significantly larger (in absolute value) than on top sites (–150 kJ/mol);<sup>17</sup> hence, the hollow sites are energetically favored over the top sites for CO adsorption on Ni(111). The adsorption site of CO has been claimed to play an important role in CO<sub>2</sub> hydrogenation on Ni nanoparticles, where the selectivity toward methane is correlated with the adsorption site and, therefore, the adsorption energy.<sup>15,27</sup> Vogt et al.<sup>15</sup> discovered that the optimal catalytic activity is achieved for a Ni particle size of 2–3 nm, which allows a relatively high amount of CO to adsorb on top sites during the hydrogenation process. The high activity of this type of adsorbed CO is attributed to its intermediate adsorption strength, facilitating further decomposition and hydrogenation toward methane. In contrast, CO adsorbed on hollow sites is more stable (due to a stronger Ni-C bond) and therefore less active. Overall, the study by Vogt et al.<sup>15</sup> highlights the close relationship between particle size effects and the presence of active surface intermediates, such as top-site CO, under reaction conditions.<sup>15</sup> Thus, understanding the mechanism of CO<sub>2</sub> activation on Ni surfaces and the influence of reaction conditions on the adsorption site of CO intermediates is not only of fundamental scientific interest but also provides valuable input for designing new catalysts and optimizing reaction conditions.

Experimental surface-sensitive techniques operating at ambient pressures can provide fundamental insights into the CO<sub>2</sub> activation mechanism on Ni surfaces. For instance, such information obtained in the millibar pressure range might give a hint about the behavior of CO<sub>2</sub> under realistic reaction pressures (1–100 bar), as sufficiently high coverage of surface intermediates can be reached under reaction temperatures, where various surface processes might be activated. So far, the interaction of CO<sub>2</sub> with model Ni catalysts under ambient conditions has been mostly studied with ambient pressure X-ray photoelectron spectroscopy (AP-XPS). Yet, the exact nature of the surface species and the chemical state of the surface are highly controversial. Yuan et al.<sup>28</sup> observed that, when Ni(111) was exposed to 0.4 mbar CO<sub>2</sub> at 25°C, the surface became highly oxidized and covered with NiO and Ni<sub>2</sub>O<sub>3</sub>. The only adsorbed species they detected on top of the oxide layer was chemisorbed CO<sub>2</sub> (CO<sub>2</sub><sup>δ-</sup>), based on their peak assignment in the C 1s region of the AP-XPS spectra. They proposed that the surface oxidation originates from the dissociative adsorption of CO<sub>2</sub>, but they did not observe adsorbed CO due to its weak binding to the oxide. In contrast, Heine et al.<sup>29</sup> found that, under ~0.3 mbar CO<sub>2</sub> in the range of 25°C–200°C, NiO is formed on the Ni(111) surface, followed by the formation of carbonate (CO<sub>3</sub><sup>2-</sup>) species via reaction of CO<sub>2</sub> with NiO.<sup>29</sup> They also attributed the oxidation of Ni(111) to dissociative adsorption of CO<sub>2</sub>, and they did not observe adsorbed CO species for the same reason as the previous study. More recently, Cai et al.<sup>30</sup> compared the interaction of CO<sub>2</sub> (~0.3 mbar) at 25°C with two different surface orientations of Ni: Ni(111) and Ni(100). They observed the formation of carbonate, adsorbed CO, and graphitic carbon on both surfaces, along with some NiO. Furthermore, they demonstrated that the surface orientation strongly affects the distribution of surface intermediates; carbonate was the dominant intermediate on Ni(111), while adsorbed CO and graphitic carbon were the major species on Ni(100). The inconsistencies in the literature regarding the observed surface species could be attributed to residual gases and issues related to the effects of ionizing radiation.<sup>31,32</sup> Such effects can be particularly significant for an active metal like Ni, as even small amounts of oxidizing or reducing residual gases can influence the chemical state of Ni surfaces.

Compared with AP-XPS, infrared (IR) spectroscopy is a less invasive technique with higher sensitivity to the molecular species and their adsorption sites. In this work, we employed polarization-modulated IR spectroscopy as the primary technique to investigate the interaction of CO<sub>2</sub> with metallic and oxidized Ni(111) model catalysts under ambient pressure and temperature conditions. Our findings offer valuable insights into the surface intermediates, adsorption sites, and chemical state of the surface. Primarily, we reveal that CO<sub>2</sub> interacts with a clean Ni(111) surface through dissociative adsorption, resulting in the formation of CO and atomic oxygen, even at 25°C. Furthermore, we found that the preferred adsorption site of CO, which is an important parameter in CO<sub>2</sub> conversion reactions, can be controlled by adjusting the sample temperature. Finally, we highlight the significant impact of residual gases on the chemical state of the Ni(111) surface under ambient CO<sub>2</sub> pressure, which might explain the discrepancies with respect to previous studies with seemingly the same Ni-CO<sub>2</sub> system.

## RESULTS AND DISCUSSION

### CO<sub>2</sub> interaction with Ni(111)

The surface intermediates that form on the Ni(111) surface in the presence of 1 mbar CO<sub>2</sub> were characterized by *in situ* polarization modulation-IR reflection absorption spectroscopy (PM-IRRAS) measurements. In each experiment, CO<sub>2</sub> was dosed at

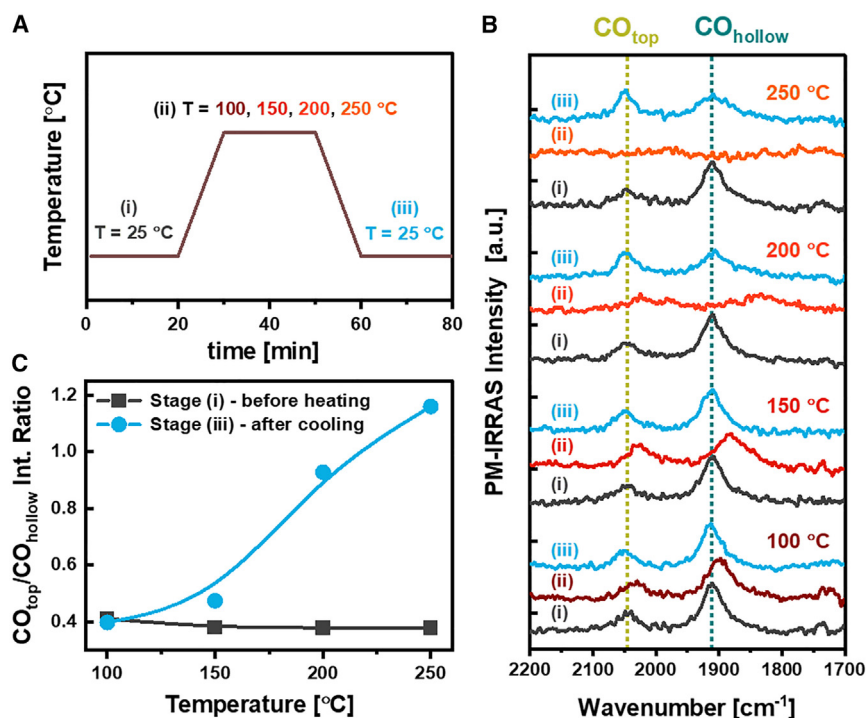


**Figure 2. PM-IRRAS characterization of CO<sub>2</sub> interaction with Ni(111)**

(A) The three-stage heating profile used during the PM-IRRAS measurements.

(B) PM-IRRAS spectra measured under a static CO<sub>2</sub> pressure of 1 mbar (dosed at 25°C).

Temperature at stage (ii) is indicated on the plots. Dashed lines label the peak positions of adsorbed CO on top and hollow sites.

(C) The initial (stage (i), before heating) and final (stage (iii), after cooling) intensity ratios of the PM-IRRAS peaks of CO<sub>top</sub>/CO<sub>hollow</sub> versus temperature.

25°C, followed by heating the sample to different temperatures between 100°C and 250°C and cooling it back to 25°C. This heating profile is illustrated in Figure 2A, whereas Figure 2B shows the baseline-subtracted PM-IRRAS spectra collected at different stages (stages (i)–(iii)) of the heating profile. Comparison of the spectra at 25°C before and after the annealing step (stages (i) and (iii)) allow us to isolate changes related to the coverage and distribution of adsorbed species from the temperature effects on the PM-IRRAS spectra. The only discernible peaks in the spectra were in the range of 1,700–2,200 cm<sup>-1</sup>. Right after CO<sub>2</sub> exposure at 25°C (stage (i) in Figures 2A and 2B), two peaks at 1,911 and 2,045 cm<sup>-1</sup> emerge in the spectrum, which we assign to the stretching frequencies of adsorbed CO on 3-fold hollow sites  $\nu(\text{CO}_{\text{hollow}})$  and top sites  $\nu(\text{CO}_{\text{top}})$ , respectively.<sup>33,34</sup> These frequencies indicate a relatively high CO coverage of  $\theta > 1/3$  monolayers (MLs) based on our calibration measurements of CO adsorption on Ni(111) (Note S1). This result demonstrates that a clean Ni(111) surface readily catalyzes the dissociation of CO<sub>2</sub> into CO and atomic oxygen at 25°C without requiring any additional thermal activation at ambient pressure. The dissociative adsorption of CO<sub>2</sub> on Ni(111) at 25°C was also observed at a much lower pressure of 10<sup>-6</sup> mbar CO<sub>2</sub> (Note S2). However, in this case, a considerably smaller  $\nu(\text{CO}_{\text{hollow}})$  peak at lower frequency was observed due to low coverage (the equilibrium coverage depends on the CO<sub>2</sub> pressure) and slower kinetics. Moreover, we verified that the observed CO in our ambient pressure experiments is indeed a product of CO<sub>2</sub> dissociation rather than a surface contaminant by performing PM-IRRAS measurements with <sup>13</sup>C-labeled CO<sub>2</sub> (<sup>13</sup>CO<sub>2</sub>). The results of these measurements are discussed in Note S3.

Upon heating the surface to different temperatures (stage (ii) in Figures 2A and 2B), notable changes are observed in the vibrational bands of CO: the bands shift to lower wave numbers, decrease in intensity, and broaden as the temperature increases. At 100°C, the  $\nu(\text{CO}_{\text{hollow}})$  and  $\nu(\text{CO}_{\text{top}})$  bands redshift to 1900 and 2032  $\text{cm}^{-1}$ , respectively, while at 150°C, they further redshift to 1,883 and 2,029  $\text{cm}^{-1}$ . At 200°C and 250°C, these CO-induced peaks become very broad and low in intensity, close to the detection limit. These frequency shifts and intensity changes are due to both a temperature effect on the vibrational bands of CO via vibrational phase relaxation<sup>33,35</sup> and a decrease in CO coverage with temperature. The latter aligns with the desorption temperature range ( $\sim 125^\circ\text{C}$ – $225^\circ\text{C}$ ) reported in previous temperature-programmed desorption (TPD) studies for CO on Ni(111), with a maximum desorption rate around 180°C.<sup>36,37</sup> The desorption temperature of CO from Ni(111) is associated with a relatively high activation energy for desorption in the range of  $\sim 85$ – $130$  kJ/mol, depending on the initial CO coverage ( $0 < \theta \leq 0.5$  ML).<sup>37</sup> Overall, the PM-IRRAS results indicate that the thermal desorption of CO, which is produced by dissociative adsorption of  $\text{CO}_2$ , is significant at 200°C and above.

Interestingly, after cooling the sample back to 25°C (stage (iii) in Figures 2A and 2B), the relative intensities of the CO peaks depend on the annealing temperature used in stage (ii). The intensity of the  $\text{CO}_{\text{hollow}}$  peak decreases with increasing annealing temperature compared with its initial intensity before heating (stage (i) in Figures 2A and 2B), while the  $\text{CO}_{\text{top}}$  peak intensity increases. The trend of the  $\text{CO}_{\text{top}}/\text{CO}_{\text{hollow}}$  intensity ratio at stage (iii) versus the annealing temperature is shown in Figure 2C. As a point of reference, the initial  $\text{CO}_{\text{top}}/\text{CO}_{\text{hollow}}$  intensity ratio before heating (stage (i)) is plotted on the same graph for each case. A similar  $\text{CO}_{\text{top}}/\text{CO}_{\text{hollow}}$  ratio of  $0.39 \pm 0.02$  is obtained in all measurements prior to heating, indicating nearly identical starting conditions, in which the preferred adsorption sites of the initially produced CO are the 3-fold hollow sites. This behavior is in line with the higher adsorption energy (in absolute values) of CO on hollow sites compared with top sites based on previous density functional theory (DFT) calculations.<sup>17</sup> Experimentally, it was also found by IR spectroscopy and XPS that CO molecules preferentially occupy hollow sites at low coverage, whereas co-adsorption on top sites takes place only at high coverage ( $0.2 < \theta_{\text{CO}} < 0.5$  ML).<sup>33,38,39</sup>

To better understand the mechanism behind the change in the preferred adsorption site of CO due to thermal annealing, we should consider the co-product of dissociative  $\text{CO}_2$  adsorption; that is, chemisorbed oxygen. We cannot monitor chemisorbed oxygen *in situ* by PM-IRRAS since the Ni-O vibration ( $\sim 560$ – $570$   $\text{cm}^{-1}$ <sup>40</sup>) is below the cutoff of our detector ( $\sim 650$   $\text{cm}^{-1}$ ), but we can account for it via *ex situ* Auger electron spectroscopy (AES) measurements in ultra-high vacuum (UHV) after evacuating the  $\text{CO}_2$ . Figure 3A shows the AES spectra measured after the PM-IRRAS experiments of  $\text{CO}_2$  adsorption at different temperatures (Figure 2) compared with a freshly prepared surface. The AES spectra obtained after  $\text{CO}_2$  adsorption at different temperatures show a small peak at  $\sim 507$  eV corresponding to the KLL transition of oxygen that is absent in the spectrum of a clean Ni(111) surface (Figure 3A). This peak arises due to all O-containing species on the surface, including both chemisorbed oxygen and CO, which are both formed by  $\text{CO}_2$  decomposition on the surface. Figure 3B (pink circles, left y axis) presents the trend of the total oxygen coverage versus annealing temperature. The oxygen coverage was evaluated from the intensity ratio of the O-KLL peak and the Ni-LMM peak ( $\sim 837$  eV) using a calibration measurement with a known oxygen coverage (Note S4). On the same graph, the  $\text{CO}_{\text{top}}/(\text{CO}_{\text{hollow}} + \text{CO}_{\text{top}})$  integrated intensity ratio obtained from

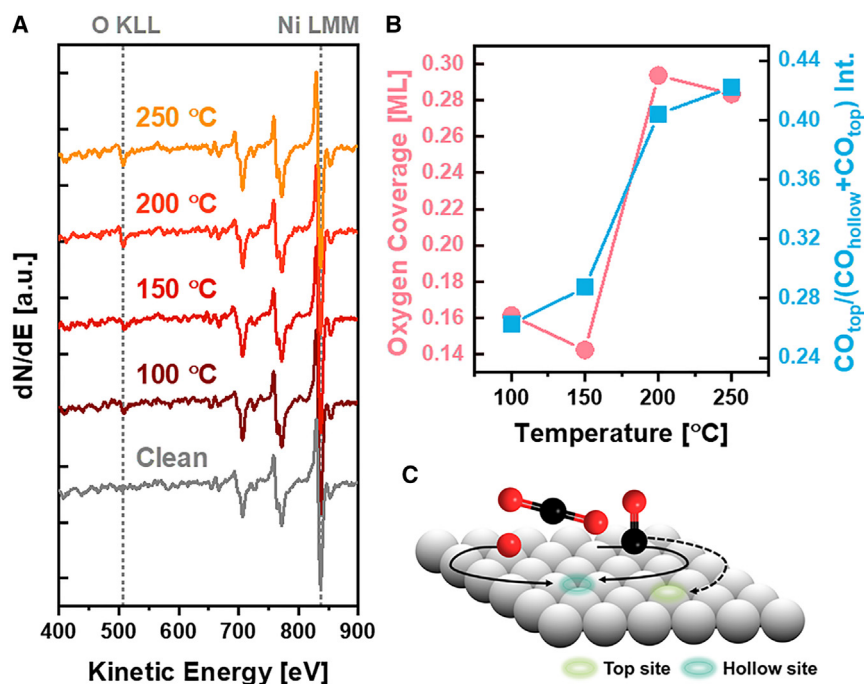


**Figure 3. Correlation between the oxygen coverage and the site distribution of CO**

(A) AES spectra of an as-prepared Ni(111) surface measured at 25°C in UHV and right after the PM-IRRAS measurements presented in Figure 2 at different temperatures (100°C–250°C).

(B) The total oxygen coverage versus annealing temperature. The coverage was estimated from the O-KLL/Ni-LMM intensity ratio based on the calibration procedure described in Note S4. For comparison, the  $\text{CO}_{\text{top}}/(\text{CO}_{\text{hollow}}+\text{CO}_{\text{top}})$  intensity ratio measured by PM-IRRAS (Figure 2) is plotted on the same graph versus temperature.

(C) Schematic of the interplay between CO and atomic oxygen produced by dissociative adsorption of  $\text{CO}_2$  on Ni(111). The solid arrows indicate that hollow sites are energetically preferred both for atomic oxygen and CO; however, CO might also adsorb on top sites (dashed arrows).

PM-IRRAS measurements (Figure 2) is also plotted (Figure 3B, light blue squares, right y axis). A correlation between the total oxygen coverage and the PM-IRRAS  $\text{CO}_{\text{top}}/(\text{CO}_{\text{hollow}}+\text{CO}_{\text{top}})$  ratio is apparent, with both exhibiting a sharp rise between 150°C and 200°C. The increase of the total oxygen coverage, assuming a similar coverage of CO (note that CO partially desorbs during pumping), can only be explained by increasing coverage of atomic oxygen with annealing temperature. The correlation between the increasing coverage of oxygen, and the site occupancy distribution of CO can be explained by competitive adsorption between CO and atomic oxygen on their most stable adsorption sites, which are the 3-fold hollow sites. This mechanism is schematically illustrated in Figure 3C. The adsorption energy of atomic oxygen (–434 to –556 kJ/mol) is significantly higher than that of CO (–145 to –202 kJ/mol).<sup>25,41–45</sup> Consequently, when CO and atomic oxygen are formed simultaneously on the surface, atomic oxygen is expected to occupy and block some of the hollow sites, forcing more of the CO molecules to adsorb on the energetically less-favored top sites. The driving force for this unique mechanism of a competitive dissociative adsorption is the relatively high coverage of CO and oxygen produced on the Ni(111) surface at ambient pressure.

The competition between CO and atomic oxygen for occupation of the hollow sites and the effect of oxygen co-adsorption on the site distribution of CO have been investigated by previous studies, where CO and  $\text{O}_2$  were dosed separately in UHV

at low surface temperatures ( $\leq 25^\circ\text{C}$ ).<sup>46–50</sup> In line with our interpretation of the results with  $\text{CO}_2$ , it was demonstrated that increasing the coverage of pre-adsorbed oxygen on Ni(111) shifts the site occupancy of CO toward top sites. Despite similar mechanism, the case of  $\text{CO}_2$  dissociation on Ni(111) at ambient conditions is substantially different from CO and oxygen co-adsorption at low temperatures in UHV. For  $\text{CO}_2$  dissociation, CO and atomic oxygen are reaction products that form simultaneously at a 1:1 ratio and within close proximity of a few angstroms from each other on the surface ( $\sim 4 \text{ \AA}$  based on DFT calculations<sup>41</sup>). These adsorption characteristics influence the CO:O ratio, the site distribution of CO, and the limiting coverage. For example, the limiting coverage is achieved once the hollow sites are fully occupied, by either oxygen or CO, so further dissociation of  $\text{CO}_2$  is hindered.

To understand the increase in oxygen coverage with increasing annealing temperature, after an initial dense layer of co-adsorbed CO and atomic oxygen has been formed at  $25^\circ\text{C}$  (stage (i) in Figure 2), the limiting step for further dissociative adsorption of  $\text{CO}_2$  on the surface has to be considered. Since CO readily forms on the Ni(111) surface at  $25^\circ\text{C}$  upon  $\text{CO}_2$  exposure, the scission of the  $\text{CO}_2$  molecule into adsorbed CO and atomic oxygen cannot be the rate-limiting step. The adsorption layer at  $25^\circ\text{C}$  should be composed of equal coverage of co-adsorbed CO and atomic oxygen, assuming that both species stay on the surface. Atomic oxygen is strongly chemisorbed exclusively on hollow sites, whereas CO is adsorbed mostly on hollow sites but also on top sites. Therefore, the hollow sites are likely to be fully occupied by either atomic oxygen or CO, preventing further  $\text{CO}_2$  dissociation. Heating the surface, especially above  $200^\circ\text{C}$  (Figure 2B), leads to desorption of CO from both top and hollow sites into the gas phase. The vacant hollow sites promote further  $\text{CO}_2$  dissociation into CO and atomic oxygen, increasing the coverage of atomic oxygen. During the cooling process (below the desorption temperature of CO), the produced CO remains on the surface; however, it is produced on an oxygen-rich surface where the predominantly available sites are the top sites. As a result, the occupancy of CO on top sites increases with annealing temperature.

The effect of annealing duration on the site occupancy of CO was examined by performing incremental heating-cooling cycles under 1 mbar  $\text{CO}_2$  at two selected temperatures:  $150^\circ\text{C}$  and  $300^\circ\text{C}$ . These temperatures were chosen because they produce a considerably different CO coverage during annealing, which markedly affects the site distribution of CO after cooling. The heating profiles and the resulting PM-IRRAS spectra at different stages are shown in Figures 4A–4C, respectively. As before, the first step of each experiment is dosing 1 mbar  $\text{CO}_2$  at  $25^\circ\text{C}$ . The  $\text{CO}_{\text{top}}/\text{CO}_{\text{hollow}}$  intensity ratio at this step (step (i), before heating) is  $\sim 0.39$ , similar to the value obtained in Figure 2. During heating cycles to  $150^\circ\text{C}$  (stages (ii), (iv), and (vi) in Figure 4B), there is still some adsorbed CO on the surface, but due to lower coverage, the  $\text{CO}_{\text{hollow}}$  and  $\text{CO}_{\text{top}}$  peak positions are redshifted to  $1,883 \text{ cm}^{-1}$  and  $2,030 \text{ cm}^{-1}$ , respectively. After each cooling cycle (stages (iii), (v), and (vii) in Figure 4B), the peak positions return back to their initial positions at  $\nu(\text{CO}_{\text{hollow}}) \sim 1,913 \text{ cm}^{-1}$  and  $\nu(\text{CO}_{\text{top}}) \sim 2,046 \text{ cm}^{-1}$ , with a  $\text{CO}_{\text{top}}/\text{CO}_{\text{hollow}}$  intensity ratio of  $0.48 \pm 0.04$ , indicating that the total CO coverage remains rather unchanged, but the  $\text{CO}_{\text{top}}/\text{CO}_{\text{hollow}}$  ratio is slightly higher compared with the initial value. During the heating cycles to  $300^\circ\text{C}$  (stages (ii), (iv), and (vi) in Figure 4C), the CO peaks completely disappear from the spectra due to complete desorption. The spectra after each cooling cycle (stages (iii), (v), and (vii) in Figure 4C) are nearly identical and contain the two peaks of  $\text{CO}_{\text{hollow}}$  and  $\text{CO}_{\text{top}}$  at  $1,908 \text{ cm}^{-1}$  and  $2,052 \text{ cm}^{-1}$ , respectively, together with an additional small peak at  $2,105 \text{ cm}^{-1}$ . This high-frequency peak has not been detected in any of our previous measurements following

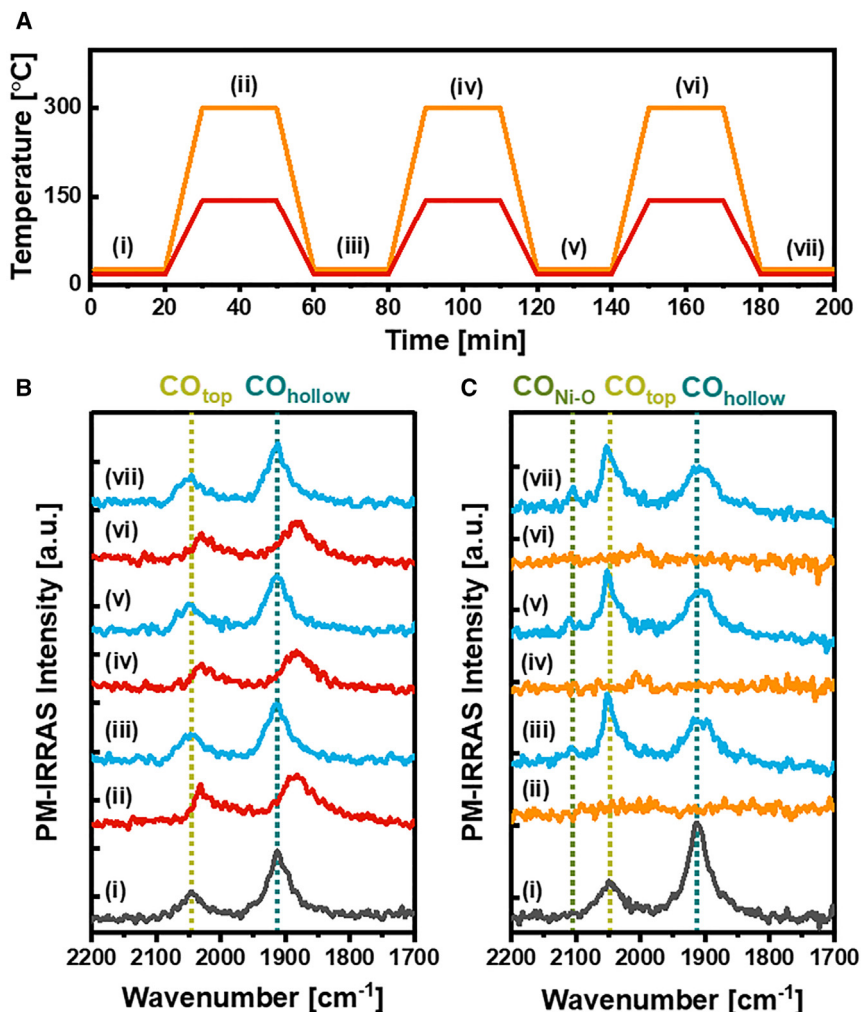


**Figure 4. CO<sub>2</sub> activation on Ni(111) under heating-cooling cycles**

(A) The heating profiles used in the PM-IRRAS experiments.

(B) PM-IRRAS spectra of Ni(111) exposed to 1 mbar CO<sub>2</sub> (dosed at 25°C) during heating-cooling cycles at 150°C.

(C) Same as (B) but for an annealing temperature of 300°C during the heating cycles. The dashed lines mark the peak positions of adsorbed CO on different surface sites.

annealing at lower temperatures (Figure 2). The obtained CO<sub>top</sub>/CO<sub>hollow</sub> intensity ratio is  $1.5 \pm 0.1$ , in agreement with the correlation between CO<sub>top</sub>/CO<sub>hollow</sub> ratio and the annealing temperature presented in Figure 2C. The slight redshift of  $\nu(\text{CO}_{\text{hollow}})$  frequency (from 1,913 cm<sup>-1</sup> to 1,908 cm<sup>-1</sup>) and the slight blueshift of  $\nu(\text{CO}_{\text{top}})$  frequency (from 2,046 cm<sup>-1</sup> to 2,052 cm<sup>-1</sup>) further support the depletion of CO from hollow sites and the increase of the CO population on top sites. The new CO stretching peak at 2,105 cm<sup>-1</sup> might be assigned to CO adsorbed on oxidized Ni sites (Ni<sup>δ+</sup>). The frequency of CO on NiO(111) film grown on an Ni(111) surface is reported as ~2,150 cm<sup>-1</sup> in the literature,<sup>51,52</sup> which is 45 cm<sup>-1</sup> higher than the value obtained here. However, it has also been mentioned that a lower stretching frequency might be obtained due to CO adsorbed on partially oxidized sites.<sup>51</sup> In addition, the exact CO stretching frequency depends on its actual coverage, which varies in different studies. It is worth noting that, despite the very low intensity of the 2,105 cm<sup>-1</sup> peak, due to the small amount of CO at these

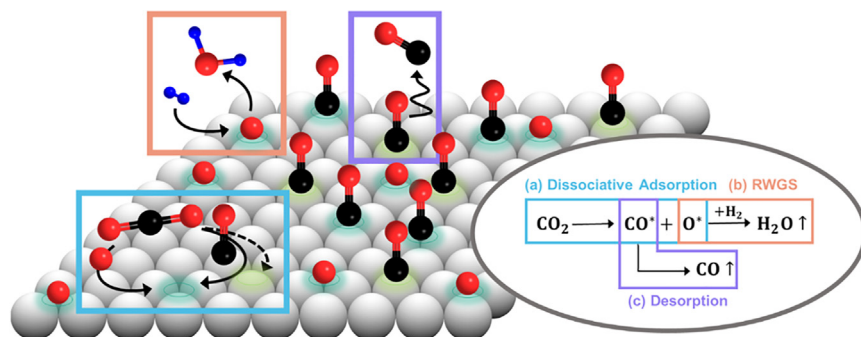


**Figure 5. Schematic of the surface processes on Ni(111) during the interaction with CO<sub>2</sub> under ambient conditions**

(A–C) (A) Dissociative adsorption of CO<sub>2</sub>, (B) RWGS, and (C) CO desorption.

sites, it is not an artifact, as its position is redshifted in test experiments with <sup>13</sup>C isotope labeling (Note S3). The appearance of CO on oxidized surface sites after annealing at 300°C supports the mechanism of increasing oxygen coverage with annealing temperature. Therefore, we believe that this peak arises due to oxidation of some of the low-coordinated Ni sites (e.g., step edges) and CO adsorption on them.

The most striking outcome of the PM-IRRAS measurements under heating-cooling cycles (Figure 4) is that the CO<sub>top</sub>/CO<sub>hollow</sub> intensity ratio after each cooling step (stages (iii), (v), and (vii) in Figures 4B and 4C) remains nearly unchanged, which means that this ratio is independent of the accumulated time at the annealing temperature. This implies that the coverage of atomic oxygen that accumulates after each annealing cycle is similar. If the opposite were true, and the oxygen coverage were to increase with every cycle, it would result in a decreasing total CO coverage and an increasing CO<sub>top</sub>/CO<sub>hollow</sub> ratio. Moreover, in this scenario, an increasing oxygen concentration in the surface/sub-surface region would lead to surface oxidation, which is not observed in the CO peak positions, indicating adsorption on a metallic Ni(111) surface. Hence, there must be a secondary process during thermal annealing that consumes atomic oxygen in parallel with its production through CO<sub>2</sub> dissociation. We propose that this process is the reduction of atomic oxygen by residual H<sub>2</sub>, which is the main background component in conventional UHV chambers and may also be present as an impurity (at the parts-per-million (ppm) level) in dosed CO<sub>2</sub> (discussed further in Note S7). This suggests that, at each annealing temperature, a steady-state coverage of atomic oxygen is achieved through a balance between three simultaneous surface reactions: dissociative adsorption of CO<sub>2</sub>, RWGS with residual H<sub>2</sub>, and thermal desorption of CO. A schematic of these reactions on Ni(111) under CO<sub>2</sub> atmosphere is presented in Figure 5. The rate constant for each reaction is determined by the surface temperature, which consequently determines the oxygen coverage in the steady state. Although, at first glance, the thermal desorption of CO may seem like a secondary process, as we mentioned before, it is most probably the bottleneck for further CO<sub>2</sub> dissociation as the presence of CO on the hollow sites blocks further CO<sub>2</sub> adsorption.

### CO<sub>2</sub> interaction with oxidized Ni(111)

Ni surfaces readily oxidize at 25°C, even at very low partial pressure of O<sub>2</sub>;<sup>40,53,54</sup> therefore, the interaction of CO<sub>2</sub> with an oxidized Ni(111) model catalyst is of particular interest. To address this, we investigated the interaction of 1 mbar CO<sub>2</sub> with

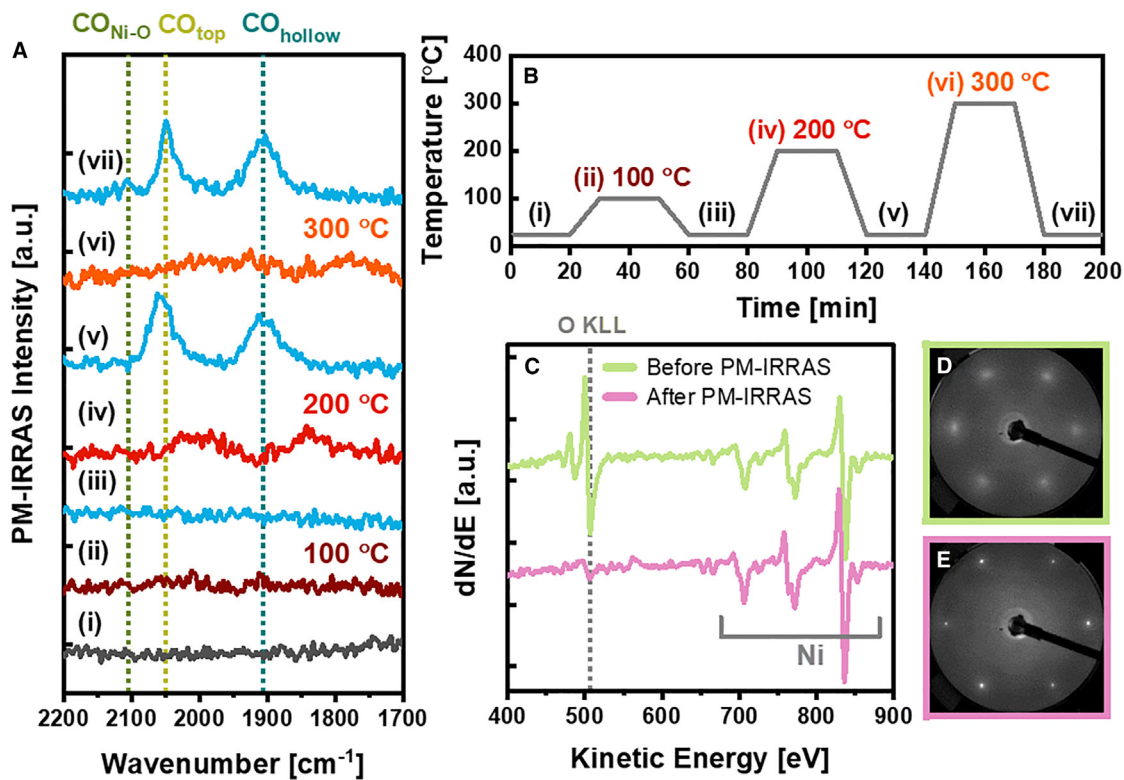


**Figure 6. CO<sub>2</sub> interaction with oxidized Ni(111) versus temperature**

(A–E) PM-IRRAS spectra of oxidized Ni(111) exposed to 1 mbar of CO<sub>2</sub> at 25°C and subsequent sequential heating to 300°C (A). The heating profile is given in (B). The Auger spectra and the LEED patterns of the oxidized Ni(111) surface before and after the PM-IRRAS measurement are presented in (C) (green) and (D) and (C) (pink) and (E), respectively.

pre-oxidized Ni(111) as a function of temperature by PM-IRRAS. The Ni(111) surface was oxidized prior to the PM-IRRAS measurements by dosing  $2.67 \times 10^{-8}$  mbar O<sub>2</sub> for 1,000 s (equivalent to 20 Langmuir (L),  $1 \text{ L} = 1.34 \times 10^{-6}$  mbar s) at 25°C. In line with the previous work of Yuan et al.,<sup>28</sup> this treatment grows a thin nanocrystalline layer of NiO(111), characterized by a low-energy electron diffraction (LEED) pattern with 6-fold rotational symmetry (Figure 6D), which has broader spots and a larger lattice parameter compared with those of the Ni(111) substrate. The distance ratio between the diffraction points  $d_{\text{Ni}(111)}/d_{\text{NiO}(111)} \sim 1.2$  (in the reciprocal space) is in good agreement with the inverse ratio of the real-space lattice parameters.<sup>28</sup>

Figure 6A shows the PM-IRRAS spectra of NiO(111)/Ni(111) under 1 mbar CO<sub>2</sub> at various temperatures, annealed and cooled according to the heating profile shown in Figure 6B. Exposing the NiO(111)/Ni(111) surface to 1 mbar CO<sub>2</sub> at 25°C did not yield any detectable peaks in the C≡O stretching region of the PM-IRRAS spectrum (Figure 6A(i)). In addition, carbonate-related peaks ( $\sim 1,500 \text{ cm}^{-1}$ ) were also not detected in the lower-frequency region of the spectrum (Figure S5). These results indicate that CO<sub>2</sub> only very weakly interacts with the oxide surface under these conditions. However, an alternative explanation might be that CO<sub>2</sub> does dissociate on the oxide but that CO, the decomposition product, is weakly bound and has a short lifetime on the surface. Heating the surface to 100°C and cooling back to 25°C did not induce any noticeable changes in the PM-IRRAS spectra (Figure 6A(ii) and (iii)); however, after heating to higher temperatures (200°C and 300°C), the peaks of adsorbed CO on top and hollow sites of Ni(111) emerged. The appearance of these

peaks implies that the thin NiO layer was reduced to metallic Ni. The AES and LEED results before and after the PM-IRRAS experiment (Figures 6C–6E) further support the reduction of the oxide layer. Before the experiment, an intense O-KLL peak (Figure 6C, green) and diffraction patterns corresponding to NiO(111) (Figure 6D) were obtained by AES and LEED, respectively. After the PM-IRRAS experiment, the O-KLL peak diminished into a much smaller peak (Figure 6C, pink), which we assign to chemisorbed oxygen, accompanied by the appearance of the diffraction spots of Ni(111) in LEED (Figure 6E). The reduction of the oxide layer under a CO<sub>2</sub> atmosphere at  $T \geq 200^\circ\text{C}$  can be attributed to the reducing effect of residual H<sub>2</sub> in the background, as we demonstrate in Note S7. The sensitivity of the Ni(111) surface to oxidation or reduction by low partial pressure of residual gases is further discussed in the next section.

### Effect of residual gases on the surface chemistry of Ni(111)

The PM-IRRAS results discussed so far have demonstrated the potential role of residual gases, specifically H<sub>2</sub>, on the chemical state of Ni(111) under CO<sub>2</sub>. The presence of residual gases in vacuum systems used for surface science techniques is inevitable, and their composition and partial pressure depend on the base pressure and the condition of the measurement chamber. Under typical UHV conditions, the main residual gases are H<sub>2</sub>, H<sub>2</sub>O, CO, and some CO<sub>2</sub>, with H<sub>2</sub> being the most abundant and CO<sub>2</sub> being the least abundant. Figure S6 shows an example of a mass spectrum measured in the vacuum chambers of the PM-IRRAS setup under a base pressure of  $\sim 10^{-10}$  mbar. When performing experiments under ambient pressure conditions, after isolating the measurement chamber from high-vacuum pumps, the partial pressure of these residual gases, as well as major air components such as N<sub>2</sub> and O<sub>2</sub> in case of small leaks, is expected to increase.<sup>55</sup> It is important to consider the effect of these residual gases in ambient pressure experiments, especially when studying reactive surfaces like Ni. In addition to H<sub>2</sub>, H<sub>2</sub>O, and CO, which principally cannot be avoided, there may be additional impurities introduced from the dosed gases (depending on the purity level) or the chamber walls due to previous experiments, further affecting the experimental results.<sup>32</sup> Based on our test experiments and previous literature, it is necessary to discuss the effects of H<sub>2</sub>, O<sub>2</sub>, H<sub>2</sub>O, and CO on the chemical state of the Ni(111) surface. These effects are likely to be the source of discrepancies observed between our PM-IRRAS results and the results of previous ambient pressure studies of the Ni-CO<sub>2</sub> system.<sup>28–30</sup>

The most critical residual gas is H<sub>2</sub> because of its abundance even in an ideal UHV chamber (Figure S6). Test experiments using AES (Note S7) demonstrate that low partial pressure of  $\sim 10^{-6}$  mbar H<sub>2</sub> (equivalent to 1 ppm from a total CO<sub>2</sub> pressure of 1 mbar) can effectively reduce thin NiO films and deplete surface oxygen. Practically,  $\sim 10^{-6}$  mbar H<sub>2</sub> and even higher cannot be avoided in ambient pressure experiments. The reduction of the NiO(111)/Ni(111) layer under a CO<sub>2</sub> atmosphere in the PM-IRRAS experiments at temperatures above 200°C (Figure 6) is attributed to residual H<sub>2</sub>, as exactly the same reduction temperature is obtained in our test experiment at  $10^{-6}$  mbar H<sub>2</sub> (Note S7). Even in excellent UHV conditions, under a base pressure of  $\sim 10^{-10}$  mbar, NiO layers can be reduced at higher temperatures; that is, with slower kinetics.

Similar to H<sub>2</sub>, CO can also act as a reducing agent or oxygen scavenger but at relatively higher pressures and temperatures.<sup>56</sup> At low partial pressure, the main impact of residual CO on Ni surfaces is strong adsorption as a contaminant. In our experiments, adsorbed CO is also the reaction product of the dissociative adsorption of

CO<sub>2</sub> on Ni(111). We verified that the observed CO in the PM-IRRAS experiments (Figure 2) is indeed a reaction product of CO<sub>2</sub> dissociation, rather than a contaminant from the background, by PM-IRRAS experiments with <sup>13</sup>C-labeled CO<sub>2</sub> (Note S3).

As low H<sub>2</sub> pressure easily reduces thin oxide films on Ni surfaces, O<sub>2</sub> can produce ordered structures of chemisorbed oxygen for very low exposure and oxide films for slightly higher exposure.<sup>40,53,54</sup> The sensitivity of a Ni(111) surface to oxidation by very low pressure of O<sub>2</sub> is demonstrated here, as exposure of 20 L O<sub>2</sub> at 25°C leads to the formation of a thin NiO(111) layer (Figure 6). Under a CO<sub>2</sub> atmosphere (1 mbar), 1 ppm of O<sub>2</sub> in the gas mixture produces an oxide layer that can be reduced by heating the surface to 200°C, while ~1,000 ppm of O<sub>2</sub> maintains the surface oxidized even at this temperature (Note S8). In agreement with the work of Mutz et al.,<sup>57</sup> we demonstrate that low levels of O<sub>2</sub> might be the reason behind Ni oxidation under ambient pressure of CO<sub>2</sub>. In the case of H<sub>2</sub>O vapor, it was found that electron beam damage may induce Ni oxidation even at an H<sub>2</sub>O pressure of 10<sup>-8</sup> mbar after a few minutes.<sup>58</sup> Here (Note S9), we tested the oxidation of Ni(111) by low pressure of H<sub>2</sub>O vapor without the external effect of an electron beam and did not observe any oxidation.

In summary, the chemical state of Ni surfaces under ambient pressure conditions is strongly influenced by the presence of residual oxidizing and reducing gases. This delicate balance between oxidizing and reducing species plays a crucial role in determining the chemical state of Ni surfaces during experiments involving CO<sub>2</sub>. In PM-IRRAS experiments, the reducing effect of background H<sub>2</sub> is the most significant factor. Even at low partial pressure (~10<sup>-6</sup> mbar), H<sub>2</sub> can effectively reduce NiO films and deplete surface oxygen, leading to a metallic Ni(111) surface.

On a final note, this study provides mechanistic insights into the activation process of CO<sub>2</sub> on Ni(111) surface under ambient conditions (1 mbar CO<sub>2</sub>, 25°C–300°C), which is an important step toward a fundamental understanding of the mechanism of CO<sub>2</sub> conversion reactions on Ni-based catalysts. However, even for the basic process of CO<sub>2</sub> activation without additional reactants, further work is required to bridge the so-called pressure and materials (structure complexity) gaps between fundamental research of model catalysts and applied catalysis.<sup>59,60</sup> For instance, here we used CO<sub>2</sub> pressure of 1 mbar, whereas CO<sub>2</sub> conversion reactions are performed at much higher pressure on the order of 10 bar, which might affect the reaction mechanism as well as the chemical state and the surface morphology. Regarding the structure complexity, here we focused on Ni(111), which is the lowest surface energy facet of Ni, but the actual surface of nanoparticle Ni catalysts is composed of different facets, such as (100), (110), and (211), and various under-coordinated surface sites depending on the size of the nanoparticle.<sup>23</sup> Hence, to elucidate the structure sensitivity of CO<sub>2</sub> activation, the interaction of CO<sub>2</sub> with different Ni surfaces has to be compared under similar conditions. On other low-index surfaces, such as Ni(100) and Ni(110), dissociative adsorption of CO<sub>2</sub> to CO and oxygen is expected to be the dominant surface process similar to Ni(111).<sup>17</sup> However, the different adsorption sites of CO and atomic oxygen on each surface might play a different role in the competitive adsorption mechanism discussed here.

In conclusion, it is demonstrated that the main reaction of CO<sub>2</sub> on Ni(111) is dissociative adsorption to CO and atomic oxygen, which takes place even at 25°C. The produced CO intermediates are distributed between hollow and top sites, and

this distribution depends on the sample temperature due to competitive adsorption between CO and atomic oxygen on the energetically preferred hollow sites. This exceptional competitive adsorption mechanism originates from the high coverage of surface intermediates obtained at ambient pressure of CO<sub>2</sub>.

A critical factor in the interaction between CO<sub>2</sub> and Ni(111) is the role of residual gases. Since CO<sub>2</sub> is a weak oxidizer, the oxidation state of Ni(111) under ambient pressure of CO<sub>2</sub> is practically determined by low concentrations of residual gases, and particularly O<sub>2</sub> and H<sub>2</sub>. The effect of residual gases is essentially important because the oxidized Ni(111) surface is inactive for CO<sub>2</sub> dissociation. We suggest that the high sensitivity of Ni surfaces to very low partial pressure of residual gases is the origin for the observed discrepancies between different ambient pressure studies of the Ni-CO<sub>2</sub> system.

The results provided in this work are significant for a basic understanding of the mechanism of CO<sub>2</sub> conversion reactions on Ni-based catalysts. Direct dissociation of CO<sub>2</sub> on Ni(111) without thermal activation or hydrogen assistance suggests that this is potentially the first step in the reaction mechanisms on industrial type Ni-based catalysts. The rapid formation of CO intermediates by CO<sub>2</sub> dissociation can affect the subsequent reaction pathway; for instance, under CO<sub>2</sub> hydrogenation conditions, this could be the first step of CO<sub>2</sub> methanation via the carbide reaction pathway or, alternatively, the first step of RWGS. Another outcome of this work is rationalizing the effect of temperature and oxygen coverage on the site distribution of CO intermediates. The adsorption site of CO correlates to its stability or reactivity; CO<sub>top</sub> is less stable than CO<sub>hollow</sub> and is considered by some researchers to be the active intermediate toward methane in CO<sub>2</sub> hydrogenation.<sup>15</sup> Therefore, manipulating the preferred adsorption site of CO by changing the reaction conditions can improve the selectivity for methane formation.

## EXPERIMENTAL PROCEDURES

### Resource availability

#### Lead contact

Requests for further information and resources should be directed to and will be fulfilled by the lead contact, Dr. Baran Eren ([baran.eren@weizmann.ac.il](mailto:baran.eren@weizmann.ac.il)).

#### Materials availability

This study did not generate new materials.

#### Data and code availability

Any additional information required to reanalyze the data reported in this paper is available from the [lead contact](#) upon request.

### Materials and experimental techniques

The interaction of CO<sub>2</sub> with Ni(111) was measured *in situ* by PM-IRRAS in a dedicated UHV setup described elsewhere.<sup>61,62</sup> Briefly, the setup consists of three chambers separated by gate valves, designated for sample introduction, preparation, and IR spectroscopy measurements (with a Nicolet iS50 Fourier transform IR [FTIR] spectrometer and mercury-cadmium-telluride detector). The exposure to CO<sub>2</sub> (Airgas USA, 99.999%) was performed in the measurement chamber, where the conditions can be switched from UHV to ambient pressure (up to 1 bar) in a static mode. For this work, a Ni single crystal with (111) orientation (99.999% purity, disk shaped with 14 mm diameter and 2 mm thickness) was obtained from Ma-Teck. Prior to the measurements, the crystal was cleaned in the preparation

chamber under a base pressure of  $2\text{--}5 \times 10^{-10}$  mbar. The cleaning procedure involved 20–30 cycles of  $\text{Ar}^+$  sputtering ( $p = 5 \times 10^{-6}$  mbar, 1.5 kV, 20–30 min), followed by annealing at  $650^\circ\text{C}$  for 10 min. The cleanliness of the surface was confirmed by obtaining sharp diffraction patterns with 3-fold rotation (quasi-hexagonal) symmetry using LEED (Figure S1). Between consecutive sets of measurements, the surface was cleaned by 2–3 cycles of sputtering and annealing. For the PM-IRRAS measurements, the cleaned Ni(111) sample was transferred in UHV to the measurement chamber, which was baked before each set of measurements to achieve a base pressure below  $1 \times 10^{-10}$  mbar. Prior to dosing  $\text{CO}_2$ , a baseline PM-IRRAS spectrum was acquired in UHV to obtain the shape of the Bessel function and ensure that the surface was free from any IR-active contaminants. Subsequently, the pumping was stopped, and the chamber was filled with  $\text{CO}_2$  at a constant pressure of 1 mbar. PM-IRRAS spectra were acquired immediately after dosing at  $25^\circ\text{C}$  and following different heating profiles with a maximum temperature of  $300^\circ\text{C}$ . A maximum dephasing ( $\phi_0$ ) of  $1,500 \text{ cm}^{-1}$  was chosen to cover the relevant frequency range for potential surface intermediates of  $\text{CO}_2$  adsorption, such as chemisorbed  $\text{CO}_2$ ,  $\text{CO}$ , and carbonate species. Each measurement consisted of 1,500 scans, taking  $\sim 20$  min, to ensure a high-quality spectrum. To remove the shape of the second-order Bessel function, the baseline spectrum measured in UHV was subtracted from the PM-IRRAS spectra measured under  $\text{CO}_2$  conditions. An example of this baseline correction can be found in Note S10.

AES and LEED measurements (with an OCI Vacuum BDL800IR device) were conducted *ex situ* in the preparation chamber before and/or after selected sets of PM-IRRAS measurements to characterize the composition and the structure of the surface. We used electron beam energies of 2,000 eV and 80–100 eV for AES and LEED, respectively.

## SUPPLEMENTAL INFORMATION

Supplemental information can be found online at <https://doi.org/10.1016/j.xcrp.2024.101890>.

## ACKNOWLEDGMENTS

This work was supported by the Israel Ministry of Energy and Infrastructure. R.B.D. acknowledges a doctoral fellowship from the Israel Ministry of Energy and Infrastructure. M.A.A. acknowledges the “la Caixa” Foundation postdoctoral fellowship.

## AUTHOR CONTRIBUTIONS

Conceptualization, R.B.D. and B.E.; methodology, R.B.D., A.B.Y., A.R.H., S.L., M.A.A., and B.E.; investigation, R.B.D., A.B.Y., A.R.H., S.L., M.A.A., and B.E.; writing – original draft, R.B.D.; writing – review & editing, R.B.D., A.R.H., M.A.A., and B.E.; funding acquisition, B.E.; resources, B.E.; supervision, B.E.

## DECLARATION OF INTERESTS

The authors declare no competing interests.

Received: December 18, 2023

Revised: February 4, 2024

Accepted: February 29, 2024

Published: March 22, 2024

## REFERENCES

- Ye, R.P., Ding, J., Gong, W., Argyle, M.D., Zhong, Q., Wang, Y., Russell, C.K., Xu, Z., Russell, A.G., Li, Q., et al. (2019). CO<sub>2</sub> hydrogenation to high-value products via heterogeneous catalysis. *Nat. Commun.* **10**, 5698. <https://doi.org/10.1038/s41467-019-13638-9>.
- Wang, M., Luo, L., Wang, C., Du, J., Li, H., and Zeng, J. (2022). Heterogeneous Catalysts toward CO<sub>2</sub> Hydrogenation for Sustainable Carbon Cycle. *Acc. Mater. Res.* **3**, 565–571. <https://doi.org/10.1021/accountsmr.2c00006>.
- Alper, E., and Yuksel Orhan, O. (2017). CO<sub>2</sub> utilization: Developments in conversion processes. *Petroleum* **3**, 109–126. <https://doi.org/10.1016/j.petlm.2016.11.003>.
- Zheng, T., Jiang, K., and Wang, H. (2018). Recent Advances in Electrochemical CO<sub>2</sub>-to-CO Conversion on Heterogeneous Catalysts. *Adv. Mater.* **30**, 18020666. <https://doi.org/10.1002/adma.201802066>.
- Wittich, K., Krämer, M., Bottke, N., and Schunk, S.A. (2020). Catalytic Dry Reforming of Methane: Insights from Model Systems. *ChemCatChem* **12**, 2130–2147. <https://doi.org/10.1002/cctc.201902142>.
- Aramouni, N.A.K., Touma, J.G., Tarboush, B.A., Zeaiter, J., and Ahmad, M.N. (2018). Catalyst design for dry reforming of methane: Analysis review. *Renew. Sustain. Energy Rev.* **82**, 2570–2585. <https://doi.org/10.1016/j.rser.2017.09.076>.
- Abdulrasheed, A., Jalil, A.A., Gambo, Y., Ibrahim, M., Hambali, H.U., and Shahul Hamid, M.Y. (2019). A review on catalyst development for dry reforming of methane to syngas: Recent advances. *Renew. Sustain. Energy Rev.* **108**, 175–193. <https://doi.org/10.1016/j.rser.2019.03.054>.
- Dorner, R.W., Hardy, D.R., Williams, F.W., and Willauer, H.D. (2010). Heterogeneous catalytic CO<sub>2</sub> conversion to value-added hydrocarbons. *Energy Environ. Sci.* **3**, 884–890. <https://doi.org/10.1039/c001514h>.
- Jiang, X., Nie, X., Guo, X., Song, C., and Chen, J.G. (2020). Recent Advances in Carbon Dioxide Hydrogenation to Methanol via Heterogeneous Catalysis. *Chem. Rev.* **120**, 7984–8034. <https://doi.org/10.1021/acs.chemrev.9b00723>.
- Zhong, J., Yang, X., Wu, Z., Liang, B., Huang, Y., and Zhang, T. (2020). State of the art and perspectives in heterogeneous catalysis of CO<sub>2</sub> hydrogenation to methanol. *Chem. Soc. Rev.* **49**, 1385–1413. <https://doi.org/10.1039/c9cs00614a>.
- Wu, H.C., Chang, Y.C., Wu, J.H., Lin, J.H., Lin, I.K., and Chen, C.S. (2015). Methanation of CO<sub>2</sub> and reverse water gas shift reactions on Ni/SiO<sub>2</sub> catalysts: the influence of particle size on selectivity and reaction pathway. *Catal. Sci. Technol.* **5**, 4154–4163. <https://doi.org/10.1039/c5cy00667h>.
- Vogt, C., Kranenborg, J., Monai, M., and Weckhuysen, B.M. (2020). Structure Sensitivity in Steam and Dry Methane Reforming over Nickel: Activity and Carbon Formation. *ACS Catal.* **10**, 1428–1438. <https://doi.org/10.1021/acscatal.9b04193>.
- Seo, H. (2018). Recent scientific progress on developing supported Ni catalysts for dry (CO<sub>2</sub>) reforming of methane. *Catalysts* **8**, 110–122. <https://doi.org/10.3390/catal8030110>.
- Vogt, C., Monai, M., Kramer, G.J., and Weckhuysen, B.M. (2019). The renaissance of the Sabatier reaction and its applications on Earth and in space. *Nat. Catal.* **2**, 188–197. <https://doi.org/10.1038/s41929-019-0244-4>.
- Vogt, C., Groeneveld, E., Kamsma, G., Nachtegaal, M., Lu, L., Kiely, C.J., Berben, P.H., Meirer, F., and Weckhuysen, B.M. (2018). Unravelling structure sensitivity in CO<sub>2</sub> hydrogenation over nickel. *Nat. Catal.* **1**, 127–134. <https://doi.org/10.1038/s41929-017-0016-y>.
- Kattel, S., Liu, P., and Chen, J.G. (2017). Tuning Selectivity of CO<sub>2</sub> Hydrogenation Reactions at the Metal/Oxide Interface. *J. Am. Chem. Soc.* **139**, 9739–9754. <https://doi.org/10.1021/jacs.7b05362>.
- Wang, S.G., Cao, D.B., Li, Y.W., Wang, J., and Jiao, H. (2005). Chemisorption of CO<sub>2</sub> on nickel surfaces. *J. Phys. Chem. B* **109**, 18956–18963. <https://doi.org/10.1021/jp052355g>.
- Álvarez, A., Borges, M., Corral-Pérez, J.J., Olcina, J.G., Hu, L., Cornu, D., Huang, R., Stoian, D., and Urakawa, A. (2017). CO<sub>2</sub> Activation over Catalytic Surfaces. *ChemPhysChem* **18**, 3135–3141. <https://doi.org/10.1002/cphc.201700782>.
- Burghaus, U. (2014). Surface chemistry of CO<sub>2</sub> - Adsorption of carbon dioxide on clean surfaces at ultrahigh vacuum. *Prog. Surf. Sci.* **89**, 161–217. <https://doi.org/10.1016/j.progsurf.2014.03.002>.
- Mohan, O., Shambhavi, S., Xu, R., Lapkin, A.A., and Mushrif, S.H. (2021). Investigating CO<sub>2</sub> Methanation on Ni and Ru: DFT Assisted Microkinetic Analysis. *ChemCatChem* **13**, 2420–2433. <https://doi.org/10.1002/cctc.202100073>.
- Schmider, D., Maier, L., and Deutschmann, O. (2021). Reaction Kinetics of CO and CO<sub>2</sub> Methanation over Nickel. *Ind. Eng. Chem. Res.* **60**, 5792–5805. <https://doi.org/10.1021/acs.iecr.1c00389>.
- Alam, M.I., Cheula, R., Moroni, G., Nardi, L., and Maestri, M. (2021). Mechanistic and multiscale aspects of thermo-catalytic CO<sub>2</sub> conversion to C1 products. *Catal. Sci. Technol.* **11**, 6601–6629. <https://doi.org/10.1039/d1cy00922b>.
- Sterk, E.B., Nieuwelink, A.E., Monai, M., Louwen, J.N., Vogt, E.T.C., Filot, I.A.W., and Weckhuysen, B.M. (2022). Structure Sensitivity of CO<sub>2</sub> Conversion over Nickel Metal Nanoparticles Explained by Micro-Kinetics Simulations. *JACS Au* **2**, 2714–2730. <https://doi.org/10.1021/jacsau.2c00430>.
- Zhou, R., Rui, N., Fan, Z., and Liu, C.J. (2016). Effect of the structure of Ni/TiO<sub>2</sub> catalyst on CO<sub>2</sub> methanation. *Int. J. Hydrogen Energy* **41**, 22017–22025. <https://doi.org/10.1016/j.ijhydene.2016.08.093>.
- Lozano-Reis, P., Prats, H., Gamallo, P., Illas, F., and Sayós, R. (2020). Multiscale Study of the Mechanism of Catalytic CO<sub>2</sub> Hydrogenation: Role of the Ni(111) Facets. *ACS Catal.* **10**, 8077–8089. <https://doi.org/10.1021/acscatal.0c01599>.
- Shah, V., Li, T., Baumert, K.L., Cheng, H., and Sholl, D.S. (2003). A comparative study of CO chemisorption on flat and stepped Ni surfaces using density functional theory. *Surf. Sci.* **537**, 217–227. [https://doi.org/10.1016/S0039-6028\(03\)00616-2](https://doi.org/10.1016/S0039-6028(03)00616-2).
- Galhardo, T.S., Braga, A.H., Arpini, B.H., Szanyi, J., Gonçalves, R.V., Zornio, B.F., Miranda, C.R., and Rossi, L.M. (2021). Optimizing Active Sites for High CO Selectivity during CO<sub>2</sub> Hydrogenation over Supported Nickel Catalysts. *J. Am. Chem. Soc.* **143**, 4268–4280. <https://doi.org/10.1021/jacs.0c12689>.
- Yuan, K., Zhong, J.Q., Zhou, X., Xu, L., Bergman, S.L., Wu, K., Xu, G.Q., Bernasek, S.L., Li, H.X., and Chen, W. (2016). Dynamic Oxygen on Surface: Catalytic Intermediate and Coking Barrier in the Modeled CO<sub>2</sub> Reforming of CH<sub>4</sub> on Ni (111). *ACS Catal.* **6**, 4330–4339. <https://doi.org/10.1021/acscatal.6b00357>.
- Heine, C., Lechner, B.A.J., Bluhm, H., and Salmeron, M. (2016). Recycling of CO<sub>2</sub>: Probing the Chemical State of the Ni(111) Surface during the Methanation Reaction with Ambient-Pressure X-Ray Photoelectron Spectroscopy. *J. Am. Chem. Soc.* **138**, 13246–13252. <https://doi.org/10.1021/jacs.6b06939>.
- Cai, J., Han, Y., Chen, S., Crumlin, E.J., Yang, B., Li, Y., and Liu, Z. (2019). CO<sub>2</sub> Activation on Ni(111) and Ni(100) Surfaces in the Presence of H<sub>2</sub>O: An Ambient-Pressure X-ray Photoelectron Spectroscopy Study. *J. Phys. Chem. C* **123**, 12176–12182. <https://doi.org/10.1021/acs.jpcc.8b11698>.
- Eren, B., and Salmeron, M. (2021). Beam-Induced Effects in Ambient Pressure Experiments with X-rays. In *ACS Symposium Series (American Chemical Society)*, pp. 249–265. <https://doi.org/10.1021/bk-2021-1396.ch010>.
- Eren, B., Ben David, R., and Shavorskiy, A. (2021). Contamination Issues in Ambient Pressure Experiments. In *ACS Symposium Series (American Chemical Society)*, pp. 267–295. <https://doi.org/10.1021/bk-2021-1396.ch011>.
- Surnev, L., Xu, Z., and Yates, J.T. (1988). Site interconversion in chemisorbed CO on Ni(111): IRAS and work function studies. *Surf. Sci.* **201**, 14–26. [https://doi.org/10.1016/0039-6028\(88\)90594-8](https://doi.org/10.1016/0039-6028(88)90594-8).
- Surnev, L., Xu, Z., and Yates, J.T. (1988). IRAS study of the adsorption of CO on Ni(111): Interrelation between various bonding modes of chemisorbed CO. *Surf. Sci.* **201**, 1–13. [https://doi.org/10.1016/0039-6028\(88\)90593-6](https://doi.org/10.1016/0039-6028(88)90593-6).
- Persson, B.N.J., and Ryberg, R. (1985). Vibrational phase relaxation at surfaces: CO on Ni(111). *Phys. Rev. Lett.* **54**, 2119–2122. [https://doi.org/10.1016/S0167-2991\(09\)61227-1](https://doi.org/10.1016/S0167-2991(09)61227-1).

36. Netzer, F.P., and Madey, T.E. (1982). The structure of CO on Ni(111). *J. Chem. Phys.* 76, 710–715. <https://doi.org/10.1063/1.442674>.
37. Miller, J.B., Siddiqui, H.R., Gates, S.M., Russell, J.N., Yates, J.T., Tully, J.C., and Cardillo, M.J. (1987). Extraction of kinetic parameters in temperature programmed desorption: A comparison of methods. *J. Chem. Phys.* 87, 6725–6732. <https://doi.org/10.1063/1.453409>.
38. Beniya, A., Isomura, N., Hirata, H., and Watanabe, Y. (2013). Displacement reaction of CO by NO on the Ni(111) surface. *Surf. Sci.* 613, 28–34. <https://doi.org/10.1016/j.susc.2013.03.001>.
39. Held, G., Schuler, J., Sklarek, W., and Steinrück, H.P. (1998). Determination of adsorption sites of pure and coadsorbed CO on Ni(111) by high resolution X-ray photoelectron spectroscopy. *Surf. Sci.* 398, 154–171. [https://doi.org/10.1016/S0039-6028\(98\)80020-4](https://doi.org/10.1016/S0039-6028(98)80020-4).
40. Tyuliev, G.T., and Kostov, K.L. (1999). XPS/HREELS study of NiO films grown on Ni(111). *Phys. Rev. B* 60, 2900–2907. <https://doi.org/10.1103/PhysRevB.60.2900>.
41. Ren, J., Guo, H., Yang, J., Qin, Z., Lin, J., and Li, Z. (2015). Insights into the mechanisms of CO<sub>2</sub> methanation on Ni(111) surfaces by density functional theory. *Appl. Surf. Sci.* 351, 504–516. <https://doi.org/10.1016/j.apsusc.2015.05.173>.
42. Catapan, R.C., Oliveira, A.A.M., Chen, Y., and Vlachos, D.G. (2012). DFT study of the water-gas shift reaction and coke formation on Ni(111) and Ni(211) surfaces. *J. Phys. Chem. C* 116, 20281–20291. <https://doi.org/10.1021/jp302488f>.
43. Zhi, C., Wang, Q., Wang, B., Li, D., and Zhang, R. (2015). Insight into the mechanism of methane synthesis from syngas on a Ni(111) surface: a theoretical study. *RSC Adv.* 5, 66742–66756. <https://doi.org/10.1039/c4ra17096b>.
44. Zhou, M., and Liu, B. (2015). DFT Investigation on the Competition of the Water-Gas Shift Reaction Versus Methanation on Clean and Potassium-Modified Nickel(111) Surfaces. *ChemCatChem* 7, 3928–3935. <https://doi.org/10.1002/cctc.201500547>.
45. Blaylock, D.W., Ogura, T., Green, W.H., and Beran, G.J.O. (2009). Computational Investigation of Thermochemistry and Kinetics of Steam Methane Reforming on Ni(111) under Realistic Conditions. *J. Phys. Chem. C* 113, 4898–4908. <https://doi.org/10.1021/jp806527q>.
46. Politano, A., and Chiarello, G. (2011). Carbon monoxide interaction with oxygenated nickel single-crystal surfaces studied by vibrational spectroscopy. *Vib. Spectrosc.* 55, 295–299. <https://doi.org/10.1016/j.vibspec.2010.12.010>.
47. Politano, A., and Chiarello, G. (2011). Vibrational investigation of catalyst surfaces: Change of the adsorption site of CO molecules upon coadsorption. *J. Phys. Chem. C* 115, 13541–13553. <https://doi.org/10.1021/jp202212a>.
48. Braun, W., Steinrück, H.P., and Held, G. (2004). The surface geometry of carbon monoxide and oxygen co-adsorbed on Ni(111). *Zeitschrift für Phys. Chemie* 218, 915–927. <https://doi.org/10.1524/zpch.218.8.915.35977>.
49. Chiarello, G., Cupolillo, A., Giallombardo, C., Agostino, R.G., Formoso, V., Pacilè, D., Papagno, L., and Colavita, E. (2003). Co-adsorption of oxygen and carbon monoxide on Ni(111). *Surf. Sci.* 536, 33–44. [https://doi.org/10.1016/S0039-6028\(03\)00573-9](https://doi.org/10.1016/S0039-6028(03)00573-9).
50. Xu, Z., Surnev, L., Uram, K.J., and Yates, J.T. (1993). Interactions between chemisorbed CO and oxygen on Ni(111). *Surf. Sci.* 292, 235–247. [https://doi.org/10.1016/0039-6028\(93\)90329-1](https://doi.org/10.1016/0039-6028(93)90329-1).
51. Bandara, A., Dobashi, S., Kubota, J., Onda, K., Wada, A., Domen, K., Hirose, C., and Kano, S.S. (1997). Adsorption of CO and NO on NiO (111)/Ni(111) surface studied by infrared-visible sum frequency generation spectroscopy. *Surf. Sci.* 387, 312–319. [https://doi.org/10.1016/S0039-6028\(97\)00366-X](https://doi.org/10.1016/S0039-6028(97)00366-X).
52. Schönnenbeck, M., Cappus, D., Klinkmann, J., Freund, H.J., Petterson, L.G.M., and Bagus, P.S. (1996). Adsorption of CO and NO on NiO and CoO: A comparison. *Surf. Sci.* 347, 337–345. [https://doi.org/10.1016/0039-6028\(95\)00997-3](https://doi.org/10.1016/0039-6028(95)00997-3).
53. Flege, J.I., Meyer, A., Falta, J., and Krasovskii, E.E. (2011). Self-limited oxide formation in Ni(111) oxidation. *Phys. Rev. B* 84, 115441. <https://doi.org/10.1103/PhysRevB.84.115441>.
54. Kortan, A.R., and Park, R.L. (1981). Phase diagram of oxygen chemisorbed on nickel (111). *Phys. Rev. B* 23, 6340–6347. <https://doi.org/10.1103/PhysRevB.23.6340>.
55. Trotochaud, L., Head, A.R., Karslioglu, O., Kyhl, L., and Bluhm, H. (2017). Ambient pressure photoelectron spectroscopy: Practical considerations and experimental frontiers. *J. Phys. Condens. Matter* 29, 053002. <https://doi.org/10.1088/1361-648X/29/5/053002>.
56. Krasuk, J.H., and Smith, J.M. (1972). Kinetics of reduction of nickel oxide with CO. *AIChE J.* 18, 506–512. <https://doi.org/10.1002/aic.690180308>.
57. Mutz, B., Gänzler, A., Nachttegaal, M., Müller, O., Frahm, R., Kleist, W., and Grunwaldt, J.D. (2017). Surface oxidation of supported Ni particles and its impact on the catalytic performance during dynamically operated methanation of CO<sub>2</sub>. *Catalysts* 7, 279. <https://doi.org/10.3390/catal7090279>.
58. Tompkins, H.G., and Scawthorn, C. (1977). The Electron Stimulated Interaction of H<sub>2</sub>O with a Nickel Surface. *Surf. Sci.* 7, 541–559. [https://doi.org/10.1016/0039-6028\(77\)90444-7](https://doi.org/10.1016/0039-6028(77)90444-7).
59. Rupprechter, G., and Weilach, C. (2007). Mind the gap! Spectroscopy of catalytically active phases. *Nano Today* 2, 20–29. [https://doi.org/10.1016/S1748-0132\(07\)70114-7](https://doi.org/10.1016/S1748-0132(07)70114-7).
60. Chen, S., Xiong, F., and Huang, W. (2019). Surface chemistry and catalysis of oxide model catalysts from single crystals to nanocrystals. *Surf. Sci. Rep.* 74, 100471. <https://doi.org/10.1016/j.surfrep.2019.100471>.
61. Ben David, R., Ben Yaacov, A., and Eren, B. (2021). Effect of Surface Orientation on Methanol Adsorption and Thermally Induced Structural Transformations on Copper Surfaces. *J. Phys. Chem. C* 125, 6099–6107. <https://doi.org/10.1021/acs.jpcc.0c10278>.
62. Ben Yaacov, A., Ben David, R., Grinter, D.C., Held, G., and Eren, B. (2021). Identification of Adsorbed Species and Surface Chemical State on Ag(111) in the Presence of Ethylene and Oxygen Studied with Infrared and X-ray Spectroscopies. *Phys. Chem.* 1, 259–271. <https://doi.org/10.3390/physchem1030020>.